In Situ X-Ray Absorption Studies on Local Structure of Annealed Metallic Glasses FeGaB and FeCoSiB

Nicolas Hayen, Philipp Jordt, Svenja C. Hövelmann, Lukas Petersdorf, Mathis Mewes, Lars Thormählen, Dirk Meyners, Nian X. Sun, Christian Sternemann, Michael Paulus, Dirk Lützenkirchen-Hecht, and Bridget M. Murphy*

The microscopic structure of Fe-based metallic glasses $(Fe_{80}Ga_{20})_{88}B_{12}$ (FeGaB) and $(Fe_{90}Co_{10})_{78}Si_{12}B_{10}$ (FeCoSiB) is investigated during in situ thermal annealing using extended X-ray absorption fine structure spectroscopy (EXAFS) above the Fe–K and Co–K absorption edges. FeGaB exhibits a phase transition above 450 °C, changing from amorphous glass to a partially crystalline structure. Its medium-range structure after this transition is modeled from crystalline α-Fe and $FeGa_3$ reference structures, combined with amorphous nearest-neighbor (NN) contributions of Fe_2B. Local order in the glass phase is described with the same model, restricted to NN interactions. Changes in the amorphous structure occur at annealing temperatures which coincide with typical observations of changes in magnetic behavior. Meanwhile, in FeCoSiB, the EXAFS response is highly different between the Fe–K and Co–K absorption edges. EXAFS oscillations on the Fe edge are strongly suppressed, as opposed to the Co edge which shows typical amplitudes. Limited resolution in this data set allows modeling only in the first amorphous shell, based on the NN distances from FeCo. The cause of the two materials' different EXAFS behavior at Fe–K despite similar iron content and identical experimental conditions is currently unknown and subject of further investigation.

1. Introduction

Metallic glasses are a family of materials characterized by the combination of metallic properties with a disordered microstructure, which gives rise to unique physical properties. They can be engineered to exhibit superior mechanical stability, corrosion resistance, or magnetic behavior and, therefore, find use in resistive coatings, transformers, and magnetic field sensors among others.[1–3] In the work of Collaborative Research Center 1261 "Biomagnetic Sensing",[4–6] metallic glasses are used as components in highly sensitive magnetic sensors tailored for biomagnetic signals, like heart signals.[7] To reach the required sensitivity in the Picotesla range,[8] special metallic glasses optimized for magnetic sensing applications are needed. The two materials $(Fe_{80}Ga_{20})_{88}B_{12}$ (FeGaB)[9,10] and $(Fe_{90}Co_{10})_{78}Si_{12}B_{10}$ (FeCoSiB)[11] are ideal candidates due to their excellent soft magnetic properties.

Understanding of the underlying atomic structure of metallic glasses and the relation with macroscopic properties is crucial in the tailoring of these sensor materials. Combined X-ray absorption near-edge structure (XANES) and extended X-ray absorption fine structure spectroscopy (EXAFS) are suitable methods for investigation of atomic short-range ordering (SRO) and medium-range ordering (MRO) around

N. Hayen, P. Jordt, S. C. Hövelmann, L. Petersdorf, M. Mewes, B. M. Murphy
Institute for Experimental and Applied Physics
Kiel University
Leibnizstraße 19, 24098 Kiel, Germany
E-mail: murphy@physik.uni-kiel.de

N. Hayen, P. Jordt, S. C. Hövelmann, L. Petersdorf, B. M. Murphy
Ruprecht Haensel Laboratory
Deutsches Elektronen-Synchrotron DESY
22607 Hamburg, Germany

The ORCID identification number(s) for the author(s) of this article can be found under https://doi.org/10.1002/pssa.202400607.

L. Thormählen, D. Meyners
Department of Materials Science
Kiel University
Kaiserstraße 2, 24143 Kiel, Germany

N. X. Sun
Electrical and Computer Engineering
Northeastern University
417 Dana Research Center, 360 Huntington Avenue, Boston
MA 02115, USA

C. Sternemann, M. Paulus
Fakultät Physik / DELTA
Technische Universität Dortmund
44221 Dortmund, Germany

D. Lützenkirchen-Hecht
Condensed Matter Physics
University of Wuppertal
Gauß-Straße 20, 42097 Wuppertal, Germany

selected elements in the compounds and have been successfully on similar Fe-rich metallic glasses.[12,13]

In this work, 1 µm thin-film samples of FeGaB and FeCoSiB are investigated with respect to temperature-dependent change in SRO during thermal annealing. As the nucleation of nanocrystallites can have a dramatic effect on the mechanical and magnetic properties,[14,15] it is necessary to understand their formation to define optimal production and operation conditions for sensors. Through an investigation with in situ XANES and EXAFS, changes in the SRO surrounding iron atoms in the compounds is determined as a function of temperature, particularly in the region of the glass transition temperature T_g. The resulting information on local structural environments can be used to deduce crystallites' composition and relative amount.[16]

2. In Situ X-ray Absorption

2.1. Absorption Spectra

Two samples were investigated for each of the two metallic glasses FeGaB and FeCoSiB. **Figure 1** shows the normalized absorption spectra of both materials at the investigated temperatures. High-temperature measurements on FeGaB include 450 and 550 °C, whereas the FeCoSiB data set contains 500 °C instead.

The main feature in both data sets is the Fe–K absorption edge at 7.1119 keV and the oscillations in the energy region beyond. The FeCoSiB data further includes additional measurements of the Co–K edge at 7.7107 keV, with an absolute height of about one-tenth of the Fe–K edge, consistent with the amount of Fe and Co in the compound. Energy calibration measurements at BL10 for the Fe–K and Co–K edges with foil reference samples show the absorption lines at 7.1131 and 7.7111 keV, revealing an edge shift of −1.2 eV for Fe–K and −0.4 eV for Co–K in the metallic glasses. The calibration data is itself shifted by +1.1 and +2.1 eV against the theoretical absorption edge positions of 7.112 and 7.709 keV.

The amplitude of the EXAFS oscillation is different for each absorption line. In FeGaB, oscillations with an amplitude of ≈1% of the edge height are observed, whereas FeCoSiB shows a similar oscillation amplitude at the Co edge, but a much weaker response at the Fe edge with less than 0.5% amplitude.
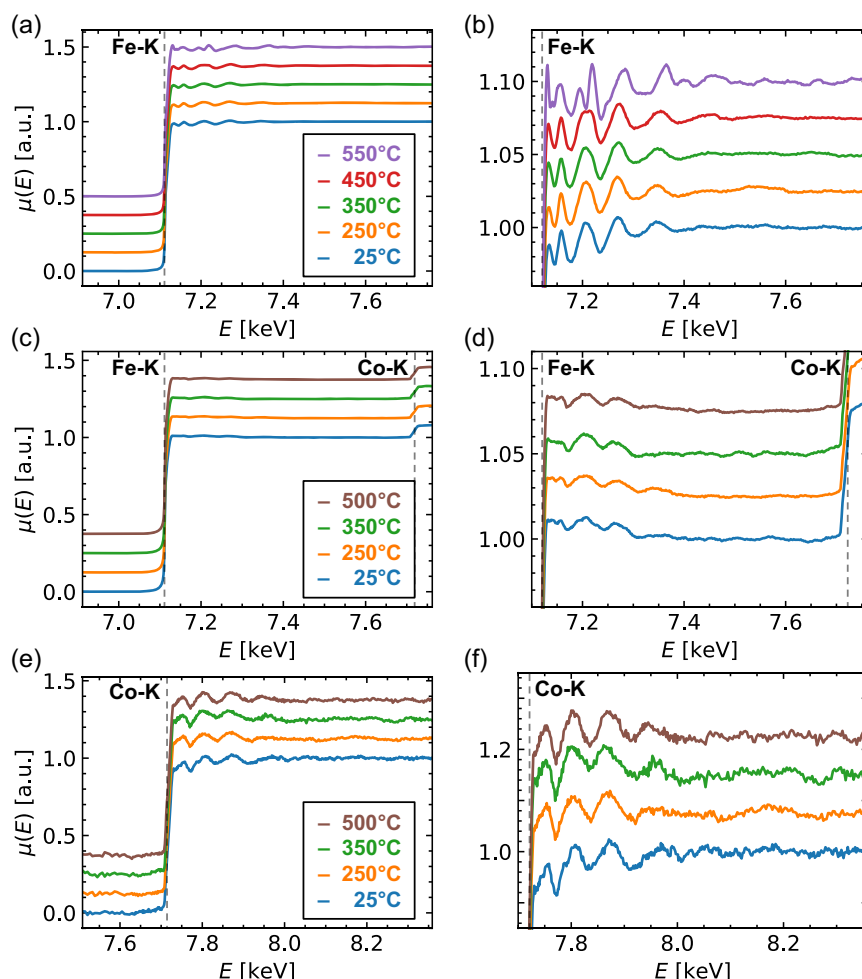
Figure 1. a,b) Normalized absorption spectra on the Fe–K edge of FeGaB and c–f) the Fe–K and Co–K edges of FeCoSiB. FeGaB at first displays post-edge oscillations up to 7.4 keV in the raw data but undergoes a phase transition between 450 and 550 °C. For FeCoSiB, Fe–K oscillations are highly suppressed and noisy, reaching only up to 7.3 keV with significantly lower amplitude while Co–K oscillations possess similar shape with high amplitude.

ADVANCED
SCIENCE NEWS
www.advancedsciencenews.com

physica
status
solidi a
www.pss-a.com

Additionally, the noise level on the FeCoSiB data is significantly higher and oscillations are suppressed 200 eV beyond either edge. In contrast, the EXAFS oscillations on FeGaB extend 350 eV past Fe–K, and even further in the 550 °C data. The change in the EXAFS pattern shape at this temperature indicates a phase transition in FeGaB to a structure with a higher degree of SRO to MRO.

The contrast in data quality at the Fe–K edge between the two materials is a very surprising result, as both materials have similar iron content of around 70% and were measured under identical experimental conditions. Additionally, at around 450 °C, a phase transition from the glass phase to a semicrystalline phase would have been expected in FeCoSiB.[11,20] The fact that the Co–K edge clearly demonstrates a degree of local order around Co atoms adds to the question as to why a similar response is absent for Fe.

The low amplitude could be attributed to the two following phenomena: first, it is plausible that a high degree of fluorescence self-absorption by FeCoSiB acts as a source of dampening for the EXAFS signal.[21] Second, a high degree of structural disorder

even within nearest-neighbor (NN) distances is a possible cause of the early cutoff for oscillations. If the SRO is dominated by local clusters with varying structure, the EXAFS response could be weakened in the ensemble average over the sample volume.

2.2. EXAFS Spectra and Fourier Transforms

From the normalized absorption data, the EXAFS spectra $\chi(k)$ and their Fourier transforms $\chi(R)$ were calculated with the Athena software, part of the Demeter package.[18] The result for both distributions for the FeGaB and FeCoSiB data is shown in **Figure 2**. The $\chi(R)$ distributions are displayed with partial phase correction of the Fourier transform, subtracting the phase shift originating from the central atom.[22] This correction shifts the distributions in R, and aligns the peaks closer to the length R_{eff} of the corresponding scattering paths.

At lower temperatures, both samples only feature one dominant peak in the radial distribution from Fe–K at ≈ 2.4 Å. The position of this feature roughly aligns with the theoretical
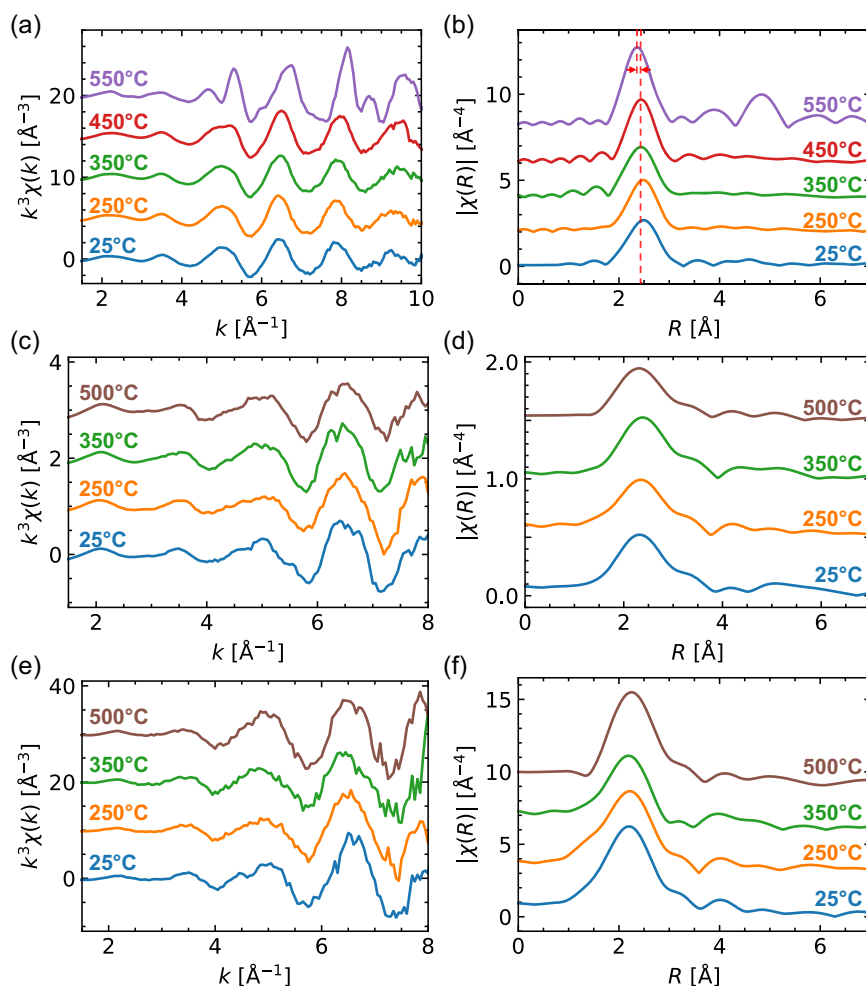
Figure 2. EXAFS spectra $\chi(k)$ and the magnitude of their Fourier transforms $\chi(R)$ calculated from a,b) the FeGaB and c–f) FeCoSiB absorption spectra in Figure 1. The Fourier transforms $\chi(R)$ are calculated with a phase correction term, which shifts the distributions to approximately align with interatomic distances. The theoretical bond lengths of Fe and Co to the other elements in either material are marked. Both materials show a single peak from the first amorphous shell. Order beyond nearest-neighbor interactions appears only in FeGaB after the phase transition at 550 °C.

2400607 (3 of 8)

bond length of Fe either to surrounding Fe atoms or the other elements in the compounds in addition to boron, which is expected at lower bond distance of 2.1 to 2.2 Å. This peak can be associated to the first coordination shell around Fe atoms in the amorphous phase.

FeGaB further shows $\chi(R)$ contributions at distances larger than the first shell after annealing at 550 °C. This indicates the emergence of longer range ordering in the surroundings of Fe atoms, that correspond to a phase transition from the glass to an at least partially crystalline phase.

The $\chi(R)$ distributions corresponding to the Co–K edge of FeCoSiB exhibit the same single amorphous peak, but with much higher magnitude and a shift in R toward a lower distance, ≈2.2 Å.

2.3. Structure Model Fitting

Further investigation of the results is possible by fitting of model structures to the $\chi(R)$ distributions of FeGaB and FeCoSiB.[19] Fitting is done using the Artemis software in the Demeter package.[18] The necessary theoretical photoelectron scattering path calculations for the different reference systems are done using the FEFF 6 code provided with Demeter.[23] The more modern FEFF 8 code for calculations is not currently available in Demeter.[24]

The number of independent parameters N_{ind} that are available to model a given data set can be determined by statistical analysis,[25,26] which is automatically considered within Artemis. In the crystalline FeGaB data, 19 independent parameters are available, while the amorphous FeGaB data can support a maximum of 11. The FeCoSiB data on either absorption edge support only 5–6 parameters individually for all temperatures; by using a fit co-refining a combined model against the Fe–K and Co–K data simultaneously, this can be improved to 11 free parameters as well.

In **Table 1**, the components of the SRO models for these four cases are outlined. Each column lists which scattering paths from each reference structure were included in the final model.

The FeGaB data model was constructed from selected scattering paths of the reference structures α-Fe, FeGa₃, and Fe₂B. For the semicrystalline phase after the transition at 550 °C, the model contains all single and multiple scattering paths from α-Fe FEFF

calculation up to a cutoff radius of 5.5 Å. Similarly, all paths from FeGa₃ are included up to 4.5 Å. The Fe₂B reference structure contributes single scattering paths from the NN Fe–B and Fe–Fe interactions.

The fits of the amorphous phases have less independent parameters available and thus require a more constrained model. The amorphous peak cannot easily be fitted to a model including multiple components, since each individual reference could fit a single peak on its own. This results in high correlations and uncertainties. In the case of FeGaB, the fitted semicrystalline structure can be used as a prior source of information to decide which reference structures need to be included in the amorphous SRO model.

The FeGaB model is adapted for the amorphous data at lower temperatures by removing Fe₂B scattering paths and lowering the cutoff radius for α-Fe and FeGa₃ to NN interactions. The model includes the Fe–Fe NN distance from α-Fe and three Fe–Ga NN distances of three nonequivalent Ga sites from FeGa₃. At 450 °C, an intermediary model is constructed that includes second NN Fe–Fe single scattering paths from both references. By excluding the longer range contributions, the amorphous data can be described while maintaining continuity between the crystalline and amorphous models.

FeCoSiB is modeled in a similar manner by consideration of NN interactions. As none of the datasets exhibit ordering beyond the first amorphous peak, it is difficult to assign multiple reference structures to the data. For this reason, to fit the Fe–K and Co–K lines, a simple model including pure α-Fe (only Fe–K), pure ε-Co (only Co–K), and FeCo (both edges) as base structures is used. All contribute only NN single scattering paths, inclusion of higher length paths negatively affects the fits. In the final model, α-Fe and ε-Co paths have been excluded because their amplitude consistently fitted to 0 in favor of FeCo for all temperatures.

The fits of the described models against the $\chi(k)$ and $\chi(R)$ distributions from Figure 2 are displayed in **Figure 3**. Best fits were selected based on the reduced χ^2 and R-factor metrics.[25] R-factor values range from 0.015 to 0.025 for FeGaB and from 0.024 to 0.062 for FeCoSiB.

A good agreement between the data and model is achieved for all $\chi(R)$ curves from Fe–K in the region of the first peak, which was weighted highest. The semicrystalline FeGaB model

Table 1. Scattering paths included in the fitting models. For each reference structure, the inclusion of single scattering (SS) and multiple scattering (MS) paths is indicated. The included range is expressed either in terms of nearest-neighbor (NN) distances or as a cutoff radius.

Reference structure	550 °C FeGaB Fe–K	Amorphous FeGaB Fe–K	FeCoSiB Fe–K	FeCoSiB Co–K
α-Fe	All SS & MS paths	1st NN Fe–Fe SS	(1st NN Fe–Fe SS)	–
	$R_{max} = 5.5$ Å	Second NN at 450 °C	Fitted to 0	–
Fe₂B	1st NN Fe–B SS	–	–	–
	1st–3rd NN Fe–Fe SS	–	–	–
FeGa₃	All SS & MS paths	1st–3rd NN Fe–Ga SS	–	–
	$R_{max} = 4.5$ Å	1st NN Fe–Fe SS at 450 °C	–	–
ε-Co	–	–	–	(1st NN Co–Co SS)
	–	–	–	Fitted to 0
FeCo	–	–	1st NN Fe–Co SS	1st NN Co–Fe SS
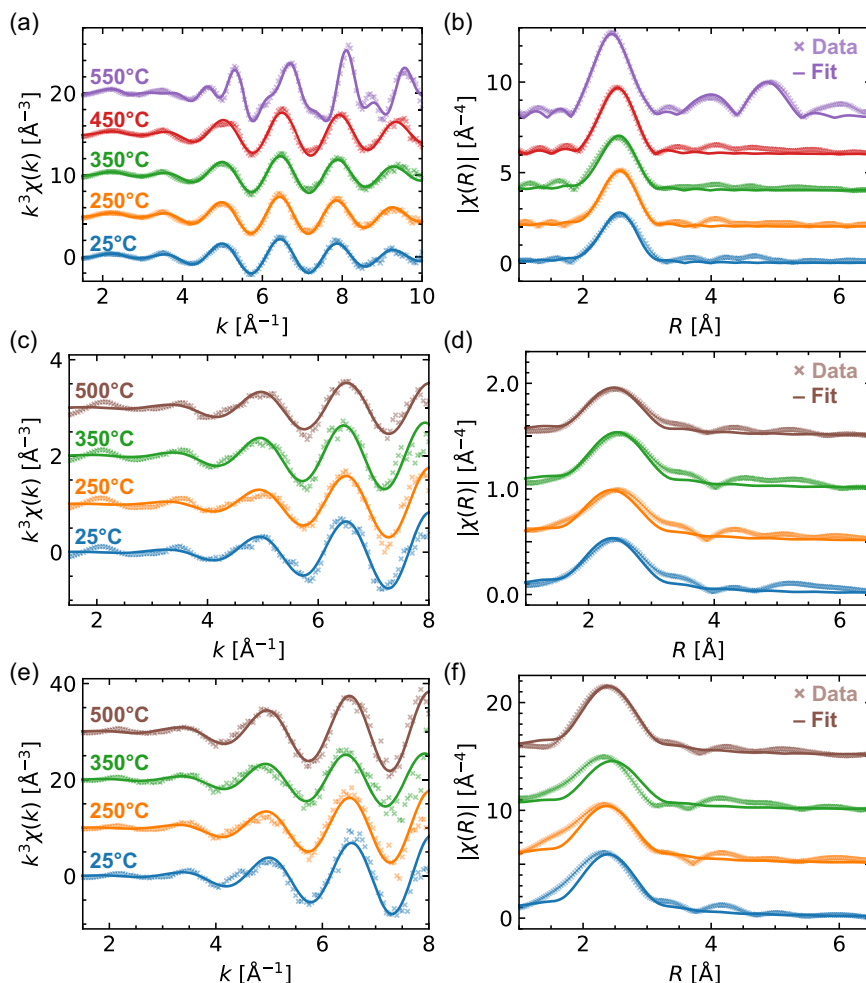
Figure 3. Structural fits of a,b) the $k^3\chi(k)$ and $\chi(R)$ distributions of FeGaB and c,d) FeCoSiB Fe–K and e,f) Co–K. Fits match the data from the Fe–K absorption edge for all temperatures, but the Co–K edge in FeCoSiB is not as well described by the used FeCo model. The 350 °C data is particularly mismatched with a visible peak displacement between data and fit.

matches the data up to the maximum distance of 5.5 Å, past which scattering paths from the references were not included in the model.

The Co–K $\chi(R)$ distribution from FeCoSiB is not described as well with the FeCo model, with significant deviations visible. Particularly striking is the fit at 350 °C, which shows significant misalignment in R between data and model. The mismatch is less obvious in $\chi(k)$, but there are phase shifts visible in the spectra from 4 to 6 Å $^{-1}$.

Temperature trends of two FeGaB model parameters are compared against values from an iron foil reference sample at room temperature in **Figure 4**. To ensure the accuracy of the reference values, Fe foil EXAFS data was sourced from the RefXAS database and fitted to pure α-Fe structure to obtain values for α_{Fe} and σ^2_{Fe}.[27,28]

The relative lattice expansion α_{Fe} and the mean square displacement σ^2_{Fe} of neighboring Fe atoms are the two parameters which apply to both crystalline and amorphous phases. The α_{Fe} data indicates that Fe–Fe distances are stretched by 3.3% in the glass phase without annealing, but gradually tend toward lower

expansion after exposure to higher annealing temperatures. With the phase transition, the lattice expansion decreases rapidly to a near-zero value, which is expected for a (partially) crystalline solid. The error bar of 0.008 in relative expansion α_{Fe} scales with R_{eff} for the absolute uncertainty ΔR. For the main peak at 2.2 to 2.4 Å in all data sets, this corresponds to an error of 0.02 Å. The mean square displacement declines more gradually toward values typical for crystalline Fe reference samples.

Both trends suggest that even before the phase transition, there is significant structural reorganization within the material during annealing. This observation is consistent with annealing studies on similar iron-rich metallic glasses,[29,30] which find changes in magnetic properties like the Curie temperature, coercive field, or saturation magnetization as a function of annealing temperature and time.

In the case of FeCoSiB, the data is limited to the amorphous phase, and a suitable model for SRO cannot be constructed from a crystalline structure. As a consequence, a number of different descriptions with nearly equivalent fit quality are possible. The simple model of FeCo is able to describe both the Fe–K and
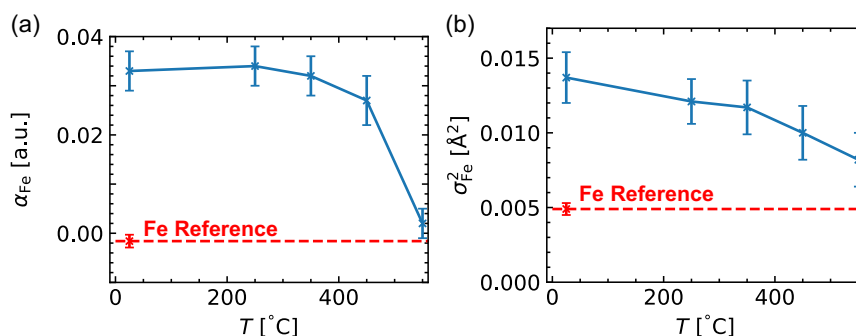
Figure 4. a) Change in relative strain α_{Fe} and b) mean square displacement σ_{Fe}^2 of Fe—Fe bonds in FeGaB as a function of temperature. Marked in red are the corresponding values obtained from an iron reference sample (data sourced from the RefXAS database[27,28]). The drop of α to near 0 coincides with the observed FeGaB phase transition. The gradual decrease of both parameters shows that reordering processes toward a more uniform SRO occur in FeGaB even before the crystallization.

Co–K $\chi(R)$ data in Figure 3 to a certain extent. The low signal to noise ratio in all FeCoSiB additionally causes parameter correlations and high relative uncertainties in the order of 100% of the fit results. It is therefore only possible to conclude the predominance of Fe atoms in the SRO of Fe and Co in FeCoSiB. Without further investigations, no other statistically significant conclusions can be drawn.

3. Conclusion

The in situ investigation of the metallic glasses FeCoSiB and FeGaB with EXAFS has revealed a significant contrast in two similar samples under identical experimental conditions. The experiment demonstrates that both materials are possible candidates for the use in biomagnetic field sensors based on their structural stability under thermal annealing. Studies of the atomic structure, for example, via X-ray diffraction and transmission electron microscopy, in combination with in situ characterization of the magnetic properties will further illuminate the role of structure in sensor functionality.

A phase transition was unambiguously observed in FeGaB between 450 and 550 °C. By modeling the SRO and MRO, the transition was identified as one from the initial glass state to a semicrystalline phase, in which α-Fe and FeGa$_3$ contribute MRO scattering and Fe–B NN distances appear. Via tracking key parameters as a function of temperature, more subtle structural changes like a gradual lattice relaxation with annealing temperature were discovered. These observations correlate to typical changes in the magnetic properties of metallic glasses during annealing below T_g, e.g., changes in Curie temperature or coercive field.[29,30]

FeCoSiB exhibited a strongly suppressed EXAFS response at the Fe–K edge, limiting the possibilities for modeling of the structure. Despite a phase transition being expected at 450 °C, the data showed only the first amorphous peak over the investigated temperature range. Using co-refinement of the EXAFS data obtained from the Fe–K and Co–K absorption lines, a model based on NN distances in FeCo was used to describe the SRO around Fe and Co atoms. The reason for the weak EXAFS at Fe–K in this sample is an open question that requires further

investigation. Potential avenues for further studies are for example an ex situ measurement of pre-annealed FeCoSiB foils, or experiments under cryogenic conditions.

4. Experimental Section

Sample Production: Metallic glass film samples were produced by radio frequency (RF) sputtering under low-pressure argon atmosphere. A 10 × 10 × 1 mm substrate of fused silica was first prepared with a 10 nm thin layer of tantalum as an adhesive before deposition of 1 μm of metallic glass. The FeGaB films were produced in collaboration with the group of Nian Sun at Northwestern University of Boston using co-deposition of Fe$_{80}$Ga$_{20}$ and B in a confocal sputtering chamber.[9,10] The FeCoSiB films were produced at Kiel University by RF sputtering of a mixed-element (Fe$_{90}$Co$_{10}$)$_{78}$Si$_{12}$B$_{10}$ target in a planar sputtering chamber.[11] Sputtering times were adjusted from[11] to enable 50 nm deposition cycles with the same cooling times. All samples were sealed under inert gas atmosphere immediately after production to avoid contact with oxygen and moisture, as both materials are extremely sensitive to corrosion.[9,11]

Measurement Setup and Procedure: The in situ EXAFS measurements were conducted at beamline BL10 at the second-generation synchrotron radiation source DELTA.[17] The wiggler provided a white X-ray beam, from which energies in the range between 4 and 16 keV could be selected via a Si (1 1 1) monochromator. Incident and transmitted X-ray intensity were monitored by N$_2$ ionization chambers directly before and after the sample stage. The photon flux at the sample position was a $\approx 3 \cdot 10^9$ photons s^{-1} mm^{-2}. The Si (1 1 1) suppressed the second harmonic of a selected energy, and the effect of higher harmonics was reduced via a combination of the limited emission from the wiggler source and low absorption in the ionization chambers at high energy giving an estimated value for the harmonic suppression of at least $5 \cdot 10^{-3}$.[17] The sample environment was an Anton Paar in situ heating cell (DHS1100), which allowed for heating up to 600 °C under rough vacuum of ≈ 1 mbar. The vacuum served to reduce exposure of the metallic glass films to oxygen and thereby prevent sample oxidation. For energy calibration of the monochromator, foil reference samples of Fe and Co were used to define the energy at the Fe–K and Co–K edges. The absorption spectra of the foils were measured in transmission geometry using the second ionization chamber directly behind the foils. Metallic glass thin-film samples were placed at an inclination of 5° to ensure full illumination with the 1 × 4.5 mm ($v \times h$) beam at a flux of about 10^{10} photons s^{-1}. The resulting X-ray fluorescence was measured using a large area passivated implanted planar silicon detector placed above the cell as close as possible to the sample. Absorption spectra were recorded by variation of the incident photon energy, ranging from 200 eV below to 650 eV above the Fe–K edge at

7.112 keV and Co–K edge at 7.709 keV, with appropriate integration time and spacing between the individual data points.

The film samples were annealed at a constant rate of $20\,°C\,min^{-1}$ up to a target temperature and held there for 10–15 min to reach thermal equilibrium. Afterward, the sample was cooled down before measuring an absorption spectrum to avoid thermal broadening of the interference patterns above the absorption edge. The same sample was then heated back up to the next highest target temperature. Investigated temperatures were in the range from 25 to 550 °C for FeGaB and 25 to 500 °C for FeCoSiB. The thin-film samples always retained damage after exposure to temperatures higher than 500 °C and subsequent cooling, with delamination of the films from their substrate likely induced by partial crystallization. This limited the access to data at high temperatures, as samples could only be treated once with elevated temperature before becoming damaged.

Data Processing: The raw signal from the fluorescence detector was normalized to the incident intensity, measured via an ionization chamber. A number of single energy points were filtered out from all data sets using a Python script; a consistent down spike in incident flux was observed at these points, which could not be fully corrected by normalization. Further processing was done using the Demeter software for EXAFS analysis.[18]

The fluorescence curves $\mu(E)$ were normalized with linear functions before and far past the Fe–K edge to ensure a step from 0 to 1. The EXAFS oscillations were then isolated from the background via a spline function; this allowed for conversion of the data from energy space to reciprocal space via Equation (1), with the electron mass m_e and the reduced Planck constant $\hbar = \frac{h}{2\pi}$. The energy constant E_0 therein was the nominal position of the absorption edge with photoelectron wave vector $k = 0$

$$k(E) = \sqrt{\frac{2m_e}{\hbar^2}(E - E_0)} \tag{1}$$

The reciprocal space spectra $\chi(k)$ obtained thorough this conversion were then further processed by weighted Fourier transformation. As a weighting function the terms k^1, k^2 and k^3 were used, where the higher-order weights served to amplify contributions at higher k. The result of the transformation was the complex distribution $\chi(R)$, with R being half the path length of a scattered photoelectron. The shape of this distribution was influenced by many parameters of the extraction process, but its magnitude could serve an indicator at which distances from a central atom other atoms were positioned on average. Therefore, it contained information about the average SRO and environment around atoms of the absorbing species. As the structure was probed by the photoelectron interaction, the accessible information was limited to the short-range regime due to the mean free path of photoelectrons.

The EXAFS spectra $\chi(k)$ and their Fourier transforms $\chi(R)$ could be compared against a theoretical model to extract structural parameters. Ab initio calculations of photoelectron scattering paths were based on ideal reference structures, and a model was built up as a linear combination of such paths from a set of possible reference structures.[19]

Individual paths were defined by four empirical fitting parameters: S_0^2 and ΔE account for scaling of the paths and a shift in E_0, respectively, and usually were global across all parts of the model. The other parameters ΔR and σ^2 were specific to each path. ΔR describes the length difference of a scattering path relative to its theoretical value R_{eff}. Finally, σ^2 is the parameter for the mean square displacement of scattering atoms on a path, including contributions from static and dynamic disorder in the material.

In the scope of this work, S_0^2 was further modified by an amplitude factor A_γ for all scattering paths originating from one reference structure γ. These factors were normalized to sum to 1 across all used references, ensuring that they acted as linear combination weights. ΔR was similarly calculated as a combination of a path's effective length R_{eff} and a parameter α_γ specific to the structure γ via $\Delta R = \alpha_\gamma \cdot R_{eff}$. This approach modeled isotropic lattice expansion or compression versus the reference with coefficient α_γ. The σ^2 parameters were constrained by assigning one to each element present in the reference structure, e.g., in the case of FeCo leading to two parameters σ^2_{Fe} and σ^2_{Co}. In the case of multiple scattering paths with different elements involved, the corresponding σ^2 value was calculated as a geometric mean of the contributing elements. In total, each reference structure included in a model required 4–6 independent parameters, depending on the number of different elements in it.

The parameterized model was then fitted against the experimental data of $\chi(R)$. To stabilize the fit against processing artifacts introduced by the extraction and transformation, a fit used the different distributions $\chi(R)$ calculated with first-, second-, and third-order k-weights simultaneously and searched for a global optimum across all three distributions. The possible model complexity was limited by the typically low number of statistically independent parameters,[19] which depended heavily on the energy range and quality of the experimental absorption spectra.

Conflict of Interest

The authors declare no conflict of interest.

Data Availability Statement

The data that support the findings of this study are openly available in [opendata@uni-kiel] at [https://doi.org/10.57892/100-72], reference number [72].

[1] R. Z. Noorbakhsh, F. Ostovan, M. Toozandehjani, *Adv. Eng. Mater.* **2024**, *26*, 2302184.

[2] J. F. Löffler, *Intermetallics* **2003**, *11*, 529.

[3] A. Hernando, M. Vazquez, J. M. Barandiaran, *J. Phys. E: Sci. Instrum.* **1988**, *21*, 1129.

[4] V. Hrkac, E. Lage, G. Köppel, J. Strobel, J. McCord, E. Quandt, D. Meyners, L. Kienle, *J. Appl. Phys.* **2014**, *116*, 134302.

[5] C. T. Koops, S. B. Hrkac, M. Abes, P. Jordt, J. Stettner, A. Petraru, H. Kohlstedt, V. Hrkac, N. Wolff, L. Kienle, O. H. Seeck, G. Nisbet, O. M. Magnussen, B. M. Murphy, in *IFMBE Proc.* (Eds: I. Tiginyanu, V. Sontea, S. Railean), Springer, Cham **2019**.

[6] P. Hayes, V. Schell, S. Salzer, D. Burdin, E. Yarar, A. Piorra, R. Knöchel, Y. K. Fetisov, E. Quandt, *J. Phys. D: Appl. Phys.* **2018**, *51*, 354002.

[7] E. Elzenheimer, P. Hayes, L. Thormählen, E. Engelhardt, A. Zaman, E. Quandt, N. Frey, M. Höft, G. Schmidt, *IEEE Sens. J.* **2023**, *23*, 5660.

[8] J. Reermann, P. Durdaut, S. Salzer, T. Demming, A. Piorra, E. Quandt, N. Frey, M. Höft, G. Schmidt, *Measurement* **2018**, *116*, 230.

[9] J. Lou, R. E. Insignares, Z. Cai, K. S. Ziemer, M. Liu, N. X. Sun, *Appl. Phys. Lett.* **2007**, *91*, 182504.

[10] J. Gao, A. Yang, Y. Chen, J. P. Kirkland, J. Lou, N. X. Sun, C. Vittoria, V. G. Harris, *J. Appl. Phys.* **2009**, *105*, 07A323.

[11] L. Thormählen, D. Seidler, V. Schell, F. Munnik, J. McCord, D. Meyners, *Sensors* **2021**, *21*, 8386.

[12] J. Zhang, G. Shan, J. Li, Y. Wang, C. H. Shek, *J. Alloys Compd.* **2018**, *747*, 636.

[13] V. A. Peña Rodríguez, J. Quispe Marcatoma, Ch. Rojas Ayala, E. M. Baggio-Saitovitch, E. C. Passamani, *J. Alloys Compd.* **2009**, *475*, 29.

[14] T. Kulik, *J. Non-Cryst. Solids* **2001**, *287*, 145.

[15] T. Brink, K. Albe, *Acta Mater.* **2018**, *156*, 205.

[16] R. Zhang, Y. Chen, Y. Fang, Q. Yu, *MRS Bull.* **2022**, *47*, 186.

[17] D. Lützenkirchen-Hecht, R. Wagner, S. Szillat, A. K. Hüsecken, K. Istomin, U. Pietsch, R. Frahm, *J. Synchrotron Radiat.* **2014**, *21*, 819.

[18] B. Ravel, M. Newville, *J. Synchrotron Radiat.* **2005**, *12*, 537.

[19] H. Joress, B. Ravel, E. Anber, J. Hollenbach, D. Sur, J. Hattrick-Simpers, M. L. Taheri, B. DeCost, *Matter* **2023**, *6*, 3763.

[20] J. Filipecki, Z. Mandecki, C. F. Conde, A. Conde, *J. Mater. Sci.* **1998**, *33*, 2171.

[21] C. H. Booth, F. Bridges, *Phys. Scr.* **2005**, *2005*, 202.

[22] B. Ravel, https://bruceravel.github.io/demeter/documents/Athena/plot/etc.html#phase-corrected-plots (accessed: October 2024).

[23] S. I. Zabinsky, J. J. Rehr, A. Ankudinov, R. C. Albers, M. J. Eller, *Phys. Rev. B* **1995**, *52*, 2995.

[24] B. Ravel, https://bruceravel.github.io/demeter/documents/DPG/feff/ (accessed: October 2024).

[25] A. Filipponi, *J. Phys.: Condens. Matter* **1995**, *7*, 9343.

[26] M. Newville, B. Ravel, D. Haskel, J. J. Rehr, E. A. Stern, Y. Yacoby, *Phys. B: Condens. Matter* **1995**, *208–209*, 154.

[27] S. Paripsa, A. Gaur, F. Förste, D. E. Doronkin, W. Malzer, C. Schlesiger, B. Kanngießer, E. Welter, J. Grunwaldt, D. Lützenkirchen-Hecht, *J. Synchrotron Radiat.* **2024**, *31*, 1105.

[28] A. Gaur, https://xafsdb.ddns.net/dataset/details/PID.SAMPLE.PREFIX5840999a-ce81-4a7d-b64f-65c1ea288b48 (accessed: October 2024).

[29] R. Sahingoz, M. Erol, M. R. J. Gibbs, *J. Magn. Magn. Mater.* **2004**, *271*, 74.

[30] T. D. Shen, B. R. Sun, S. W. Xin, *Intermetallics* **2015**, *65*, 111.